

This is the accepted manuscript made available via CHORUS. The article has been published as:

Compton profile of $\text{VO}_{\{2\}}$ across the metal-insulator transition: Evidence of a non-Fermi liquid metal

Ilkka Kylänpää, Ye Luo, Olle Heinonen, Paul R. C. Kent, and Jaron T. Krogel

Phys. Rev. B **99**, 075154 — Published 26 February 2019

DOI: [10.1103/PhysRevB.99.075154](https://doi.org/10.1103/PhysRevB.99.075154)

Compton profile of VO₂ across the metal-insulator transition: evidence of a non-Fermi liquid metal*

Ilkka Kylänpää^{1,†}, Ye Luo², Olle Heinonen^{3,4}, Paul R. C. Kent^{5,6}, and Jaron T. Krogel¹

¹*Materials Science and Technology Division, Oak Ridge National Laboratory, Oak Ridge, Tennessee 37831, USA*

²*Computational Science Division, Argonne National Laboratory, Lemont, Illinois 60439, USA*

³*Materials Science Division, Argonne National Laboratory, Lemont, Illinois 60439, USA*

⁴*Center for Hierarchical Material Design, Northwestern-Argonne Institute for Science and Engineering, Northwestern University, Evanston, Illinois 60208, USA*

⁵*Center for Nanophase Materials Sciences, Oak Ridge National Laboratory, Oak Ridge, Tennessee 37831, USA and*

⁶*Computational Sciences and Engineering Division, Oak Ridge National Laboratory, Oak Ridge, Tennessee 37831, USA*

(Dated: January 29, 2019)

Many-body diffusion Monte Carlo is used to obtain first-principles momentum distribution and Compton profile of vanadium dioxide. Our results for the Compton profile are in good agreement with the experimental values, and we show that a good qualitative agreement in scaled Compton profile difference across the monoclinic to rutile phase transition depends on an accurate description of electron correlation. The electron momentum distribution enables new insights into the metal-insulator phase transition. For example, the probability for electron scattering in the proximity of the Fermi surface (forward scattering) is suppressed in the vanadium chain direction (rutile *c*-axis), but enhanced in perpendicular directions. However, along the *c*-axis we observe an increase at $\sim 2k_F$ in the momentum distribution, which is characteristic for Friedel oscillations (back scattering). Our analysis of the momentum distribution supports experimentally observed anisotropies and provides an explanation for the anomalously low electronic thermal conductivity observed recently in the metallic phase [Lee *et al.* Science 355, 371 (2017)]. Moreover, our results indicate non-Fermi liquid behavior as well as quasi-1D Friedel oscillations in the metallic rutile phase, which is reminiscent of a Tomanaga-Luttinger liquid with impurities.

I. INTRODUCTION

Vanadium dioxide (VO₂) is an amphoteric oxide with functional properties suitable for various solid state applications including glass optics, ceramic applications, data storage, and fast optical shutters [1]. It has also become known as a prototypical strongly correlated electron material that challenges theoretical and computational modeling [2–6]. For example, despite its success with various materials, density functional theory (DFT) has not been able to adequately capture the electronic and magnetic structures of VO₂ [7]. This is in part due to electronic correlations that DFT does not capture accurately [8]. In 2015 Zheng and Wagner [9] demonstrated the need for a higher accuracy many-body approach, i.e. quantum Monte Carlo (QMC), to correctly describe the electronic

and magnetic structures of VO₂. Accurate spectral properties, however, have successfully been obtained by beyond DFT approaches such as dynamical mean field theory (DMFT) [10–12] and many-body perturbation theory (GW) [13, 14].

The wealth of interest for VO₂ stems from its rich phase diagram with desirable properties controllable, e.g., by temperature, pressure and doping [15–22]. Here we focus on the thermally induced metal to insulator transition (MIT) from insulating monoclinic phase (M1, $T < T_c$) into a metallic rutile phase (R, $T > T_c$) [23–25]. This tunable MIT is accompanied by a change in the underlying crystal lattice structure, which at ambient pressure occurs at $T_c \approx 341$ K for pure unstrained VO₂. This transition has been very recently studied with Compton profile measurements [26], which revealed a poor correspondence between the experiments and theoretical DFT results. Moreover, the high-temperature metallic phase was observed recently to exhibit a peculiar non-Fermi liquid character and anomalously low electronic thermal conductivity [15]. Earlier experiments had already shown a strong anisotropy in the metallic phase, with the conduction along the rutile *c*-axis suppressed compared to the perpendicular directions [27]. We use the momentum distribution $n(k)$ and Compton profile $J(q)$ to address the transition, and the nature of the metallic R phase: is it a normal Fermi liquid, and what signatures do $n(k)$ and $J(q)$ reveal?

Both the momentum distribution and Compton profile are powerful probes for understanding the ground state properties of materials. The momentum distribution of

* This manuscript has been authored by UT-Battelle, LLC under Contract No. DE-AC05-00OR22725 with the U.S. Department of Energy. The United States Government retains and the publisher, by accepting the article for publication, acknowledges that the United States Government retains a non-exclusive, paid-up, irrevocable, worldwide license to publish or reproduce the published form of this manuscript, or allow others to do so, for United States Government purposes. The Department of Energy will provide public access to these results of federally sponsored research in accordance with the DOE Public Access Plan (<http://energy.gov/downloads/doe-public-access-plan>).

[†] ilkka.kylanpaa@tuni.fi; Present address: Computational Physics Laboratory, Tampere University, P.O. Box 692, 33014 Tampere, Finland

the electrons can be experimentally studied by scattering methods such as Compton scattering, positron annihilation, the $(e, 2e)$ process and high energy electron scattering [28–31]. In general, the differential cross sections can be related to the momentum distribution. For Compton scattering this requires an assumption that the transferred energy and momentum are high compared to those characteristic to the ground state properties and collective behavior. This assumption results in the “Impulse Approximation” (IA) in which, e.g., the Compton profile as well as the dynamical structure factor are proportional to the projection of $n(k)$ onto a scattering vector [32, 33]. Within the IA directional Compton profile in z -direction is given as

$$J(q) = \iint n(k_x, k_y, k_z = q) dk_x dk_y. \quad (1)$$

The IA is especially appropriate for X-ray Compton scattering from electronic systems [30, 32], and thus, it is capable of providing a unique perspective for understanding the electronic structure of materials; the properties of the bulk, in particular.

In normal Fermi liquids, the electron momentum distribution has a discontinuity at the Fermi momentum k_F . In three-dimensional systems this discontinuity defines the shape of the Fermi surface, which is also related to the screening properties of the electrons [34]. The magnitude of the discontinuity at the Fermi surface, on the other hand, quantifies the strength of a quasiparticle excitation and is called the renormalization factor (Z) [35, 36]. For strongly coupled systems Z tends to zero as the coupling strength increases, which can be used as a measure of electron correlations. In the case of superfluidity or superconducting behavior the Fermi surface actually disappears, and the discontinuity is absent also in some semi-metals [32]. Interestingly, even the smallest amount of interaction will destroy the discontinuity in $n(k)$ in one-dimensional chains according to the Tomanaga-Luttinger theory [37–39]. Broadening of the sharp drop at k_F is also associated with the opening of a band gap [40]. To this end, the momentum distribution provides complementary, and possibly even more informative, knowledge to other characterizations of many-body systems.

Here we will first motivate the use of our first-principles approach, i.e., quantum Monte Carlo (QMC), and discuss computational details. Second, we will show that our QMC results are in excellent *qualitative* agreement with recent experimental data [26] on the scaled Compton profile difference across the MIT. Third, we will address the origin of the *quantitative* discrepancy between theory and experiment. Then we will consider the subtle details of the momentum distribution across the MIT and in individual phases (R phase in particular), and explain possible implications to the underlying physics. This analysis is further tied in with insights obtained from post-processed electron densities of Ref. [8].

II. METHODS AND COMPUTATIONAL DETAILS

Using continuum diffusion Monte Carlo (DMC) [41–43] we are able to obtain the momentum distribution function from first principles. This is accomplished by evaluation of the expectation value

$$n(\mathbf{k}) = \Omega^{-1} \sum_{j=1}^N \left\langle \int d\mathbf{s}_j \frac{\Psi(R + \mathbf{s}_j)}{\Psi(R)} e^{-i\mathbf{k} \cdot \mathbf{s}_j} \right\rangle_{|\Psi(R)|^2}, \quad (2)$$

where Ω is the volume containing N electrons, R includes the coordinates of all the electrons, and \mathbf{s}_j is a displacement vector acting on the j^{th} electron. The DMC approach is known for its accuracy in solving ground state electronic structure properties for both molecular and solid state systems from first principles [9, 42, 44–46]. In particular, DMC straightforwardly and accurately includes electron correlations [47–49]. Importantly, in recent years it has been demonstrated that the challenges introduced by electron correlation and the description of 3d orbitals of transition metal oxides are overcome by DMC [49–64]. Therefore, QMC is regarded as an excellent computational tool for validating and predicting material properties. Use of QMC in periodic supercells results in finite size effects, but unexpectedly, we find that these are small for $n(k)$ in VO_2 , which differs from past experience with the homogeneous electron gas [36, 65].

Crystal structures for the M1 [66] and R [67] phases were obtained from the Inorganic Crystal Structure Database [68]. All calculations were performed with the experimental lattice constants. In both phases, the vanadium atoms are arranged in quasi-1D chains and, as in Ref. [9], an antiferromagnetic ordering was imposed by fixing alternating up/down spin moments along the chains. More details on the experimental lattice vectors and atomic coordinates of the M1 and R crystal structures are given below regarding our density functional theory (DFT) and quantum Monte Carlo (QMC) calculations. In addition, full simulation inputs and outputs for all QMC and DFT calculations performed in this work are available via the Materials Data Facility [69] (DOI: provided upon acceptance).

A. Density functional theory

Our density functional theory (DFT) calculations were performed in the antiferromagnetic (AFM) magnetic primitive cell of VO_2 (4 VO_2 formula units for M1 and R). We used experimental crystal structures [66, 67] from the Inorganic Crystal Structure Database (ICSD). See Table I for information on the axes and atomic positions. In Table I we use V1 and V2 when referring to the different magnetic orientations of the Vanadium atoms (spin up and spin down, respectively). We used plane-wave energy cutoffs of 350 Ry with $12 \times 12 \times 24$ and $24 \times 12 \times 12$ k -space grid for R phase and M1 phase, respectively. The DFT

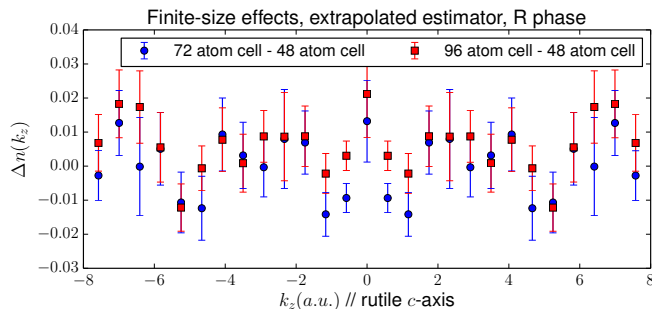


FIG. 1. Finite-size effects on the momentum distribution considered as the difference between 72 atom and 48 atom as well as 96 atom and 48 atom supercells.

calculations were performed with Quantum Espresso [70] using hard norm-conserving pseudopotentials as in our earlier study [8].

B. Quantum Monte Carlo

The quantum Monte Carlo simulations were carried out with QMCPACK [43, 71] in a supercell containing 16 VO_2 formula units, that is, 48 atom supercell. The experimental crystal structures used in DFT calculations were tiled to give the supercells described in Table II. For faster convergence to thermodynamic limit, we used twist-averaged boundary conditions [72] with a $4 \times 4 \times 4$ supercell twist angle grid instead of purely periodic boundary conditions. This also results in better resolution for the momentum distribution. In order to estimate the finite-size effects on the momentum distribution we performed additional simulations for the R phase for 72 and 96 atom supercells. We find that the momentum distribution is well converged already with our 48 atom supercell. This can be seen in Fig. 1, where we show the difference between the larger supercells and the 48 atom cell along the rutile c -axis. The differences show no consistency to increase or decrease, and the magnitude is small also; roughly zero within two standard deviations.

The trial wavefunction (Ψ_T) used is of the standard Slater-Jastrow [73, 74] type:

$$\Psi_T = \det\{\psi_\uparrow\} \det\{\psi_\downarrow\} e^J. \quad (3)$$

The purpose of the trial wavefunction is to guide the simulation both more accurately and more rapidly to the ground state. A trial wavefunction with a better nodal surface—arising from the sets of orbitals above—leads to a more accurate diffusion Monte Carlo (DMC) result. A trial wavefunction with a better Jastrow factor improves the timestep and pseudopotential localization approximations made in DMC and also reduces the statistical variance, making the calculations more efficient. Since a good trial wavefunction is important in improving the approximations made in DMC, we describe in more detail

below how we obtained an optimal wavefunction within the Slater-Jastrow ansatz.

The product of spin-up and spin-down determinants of spatial orbitals arise from a single determinant of spin-orbitals after fixing the electron spins, while the overall state is a spin-unrestricted antiferromagnet [51]. The determinants are composed of single particle orbitals taken from spin-unrestricted LDA+U (via Quantum Espresso), in which the correct magnetic structure was imposed by initializing the magnetic moments in an antiferromagnetic configuration along the V-V chains. Convergence to the AFM state was further confirmed after the self-consistent density functional theory calculations by analysis of the magnetic structure and spin-resolved Löwdin charges.

In the Jastrow factor (e^J) we include terms up to two-body (electron-electron) correlation functions, i.e.,

$$J = J_1 + J_2 \\ = \sum_{I,i} u_1(|r_i - R_I|) + \sum_{i < j} u_2(|r_i - r_j|), \quad (4)$$

where r_i and R_I refer to electron and ion coordinates, respectively. The u_1 and u_2 , correlation functions depend, as appropriate, on both the ionic and spin species involved. The functions u_1 and u_2 are parameterized in terms of radial B-splines [75].

The Jastrow parameters were optimized by making use of the variational principle as applied to the total energy and the energy variance. The optimization was performed by minimizing a cost function containing a 95/5 ratio of energy and variance with the linear method [76], which results in a good balance between improvements in DMC pseudopotential localization approximation [77–79] and the resulting variance of the local energy [80]. We optimize the Jastrow part only with variational Monte Carlo (VMC), which improves the description of particle-particle correlations, but does not modify the nodal surface. The orbitals are instead optimized directly with DMC, though within the restricted variational freedom afforded by LDA+U.

In DMC the operator $\exp[-\tau(\hat{H} - E_T)]$ is used to project out the lowest eigenstate that has non-zero overlap with the chosen fixed node / trial wave function [42], where \hat{H} is the many body Hamiltonian and E_T is an estimate of the ground state energy, which is updated throughout the simulation. In our earlier work [8] the DMC fixed node/phase error [81–83] was minimized by using the Hubbard-U value as a variational parameter optimized directly in DMC, with $U = 3.5$ eV yielding the lowest energy. In production runs, the DMC timestep was set to 0.005 Ha^{-1} , resulting in an acceptance ratio greater than 99.6%. Non-local pseudopotentials were handled in the DMC projector within the variational T-moves scheme [79, 84].

Since DMC provides a “mixed” estimate of the momentum distribution (a mixture between the fixed node estimate and the VMC one), we have corrected the mixed

estimates by extrapolation to obtain “pure” estimates of the momentum distribution, reflecting the fixed node wave function (Φ) alone. This is a general property of the DMC method for operators that do not commute with the Hamiltonian. In order to obtain pure estimates of the momentum distribution ($n(k)$), we used the extrapolation formula [42]:

$$n_{\text{extrap}} = 2n_{\text{DMC,mixed}} - n_{\text{VMC}} + \mathcal{O}((\Phi - \Psi_T)^2). \quad (5)$$

C. Momentum distribution and Compton profile

Momentum distribution $n(\mathbf{k})$ is obtained by taking the Fourier transform of the one-body density matrix:

$$\begin{aligned} n(\mathbf{k}) &= \frac{N}{\Omega} \int d\mathbf{R} d\mathbf{r}'_1 e^{i(\mathbf{r}_1 - \mathbf{r}'_1) \cdot \mathbf{k}} \rho(\mathbf{r}_1, \dots, \mathbf{r}_N, \mathbf{r}'_1, \dots, \mathbf{r}_N) \\ &= \frac{N}{\Omega} \int d\mathbf{s} e^{-i\mathbf{k} \cdot \mathbf{s}} n(\mathbf{s}), \end{aligned}$$

where N is the number of electrons, $\mathbf{R} = \{\mathbf{r}_1, \dots, \mathbf{r}_N\}$, $\mathbf{s} = \mathbf{r}'_1 - \mathbf{r}_1$, and

$$n(\mathbf{s}) = \int d\mathbf{R} \rho(\mathbf{r}_1, \dots, \mathbf{r}_N, \mathbf{r}_1 + \mathbf{s}, \dots, \mathbf{r}_N).$$

In variational Monte Carlo (VMC) and diffusion Monte Carlo (DMC)

$$\begin{aligned} n(\mathbf{s}) &= \int d\mathbf{R} \Psi^*(\mathbf{r}_1, \dots, \mathbf{r}_N) \Psi(\mathbf{r}_1 + \mathbf{s}, \dots, \mathbf{r}_N) \\ &= \int d\mathbf{R} |\Psi(R)|^2 \frac{\Psi(R')}{\Psi(R)}, \end{aligned}$$

which gives us

$$n(\mathbf{k}) = \int d\mathbf{R} |\Psi(R)|^2 \frac{N}{\Omega} \int d\mathbf{s} \frac{\Psi(R')}{\Psi(R)} e^{-i\mathbf{k} \cdot \mathbf{s}}.$$

In practice, the above will be estimated through

$$n(\mathbf{k}) = \left\langle \frac{N}{\Omega} \frac{1}{N_s} \sum_{j=1}^{N_s} \frac{\Psi(R')}{\Psi(R)} e^{-i\mathbf{k} \cdot \mathbf{s}_j} \right\rangle_{|\Psi(R)|^2}, \quad (6)$$

where N_s refers to the number of samples used in the Monte Carlo integral for $\int d\mathbf{s}$. Notice that the momentum distribution normalizes to the number of electrons

$$\sum_{\mathbf{k}} n(\mathbf{k}) = N = \frac{\Omega}{(2\pi)^d} \int d\mathbf{k} n(\mathbf{k}) = \int d\mathbf{k} \tilde{n}(\mathbf{k}), \quad (7)$$

in which a finite system and a system at the thermodynamic limit are described by summation and integration, respectively, and $\tilde{n}(\mathbf{k}) = (2\pi)^{-d} \Omega n(\mathbf{k})$.

The Compton profile is obtained as an integral of the momentum distribution [30]. For example, the directional Compton profile in the z -direction is given as

$$J(q) = \int dk_x dk_y \tilde{n}(k_x, k_y, k_z = q). \quad (8)$$

In the spherically symmetrized (or isotropic) case we have

$$\begin{aligned} J(q) &= \frac{1}{2} \int_{|q|}^{\infty} dk \frac{1}{k} I(k) \\ &= \frac{1}{2} \int_{|q|}^{\infty} dk \frac{1}{k} 4\pi k^2 \tilde{n}(k) \\ &= 2\pi \int_{|q|}^{\infty} dk k \tilde{n}(k) \end{aligned} \quad (9)$$

with $I(k) = 4\pi k^2 \tilde{n}(k)$. Also the Compton profile normalizes to the number of electrons, i.e.,

$$\int_{-\infty}^{\infty} dq J(q) = N. \quad (10)$$

In practice with periodic simulations we need to resort to a finite number of k -points in which we describe the momentum distribution. This introduces a cut-off (k_c) into our k -grid. Let's consider this in the case of spherically symmetric (or angular averaged) momentum distribution and the related Compton profile. According to Eq. (7) we can write

$$\begin{aligned} N &= \int d\mathbf{k} \tilde{n}(\mathbf{k}) \\ &= \int_0^{k_c} dk 4\pi k^2 \tilde{n}(k) + \Delta N. \end{aligned} \quad (11)$$

Considering large enough k_c we can approximate the tail by a decaying function such as $A \exp(-Bk)/k$, and thus,

$$\begin{aligned} \Delta N &= \int_{k_c}^{\infty} dk 4\pi k^2 \tilde{n}(k) \\ &\approx \int_{k_c}^{\infty} dk 4\pi k A e^{-Bk} \\ &= \frac{4\pi A}{B^2} [1 + Bk_c] e^{-Bk_c}. \end{aligned} \quad (12)$$

Therefore, in optimizing the coefficients for the tail it is also possible to use the accuracy in ΔN as a constraint in addition to the few points at the tail.

For the “isotropic” Compton profile this yields

$$J(q) = 2\pi \int_{|q|}^{\infty} dk k \tilde{n}(k) = 2\pi \int_{|q|}^{k_c} dk k \tilde{n}(k) + \Delta J, \quad (13)$$

where

$$\Delta J = 2\pi \int_{k_c}^{\infty} dk k \tilde{n}(k) \approx \frac{2\pi A}{B} e^{-Bk_c}. \quad (14)$$

Notice that for $q \geq k_c$ the tail of the “isotropic” Compton profile can be approximated by Eq. (14). This can be used in the calculation of the norm of the Compton profile in the range $(-\infty, \infty)$:

$$N = \int_{-\infty}^{\infty} dq J(q) = 2 \int_0^{q_c} J(q) + 2\Delta N, \quad (15)$$

where the “correction term” (ΔN) to the norm is given by

$$\Delta N = \int_{k_c}^{\infty} dq \Delta J \approx \frac{2\pi A}{B^2} e^{-Bk_c}. \quad (16)$$

Another aspect arising from periodic simulations might be harder to notice, but it can be dealt with by converging the trial wave function with a set of k-points that include your desired k-grid. That is, already at the DFT level the SCF calculation should include the k-points that will be used in the NSCF calculation for the trial wave function. Failing to do this would lead to some sort of “interpolation” between the k-points of the SCF calculation, which can introduce subtle, but noticeable, inconsistencies—at least in the momentum distribution. In Compton profile these small inconsistencies would, however, be suppressed due to the integration, and thus, the Compton profile would be less affected by this.

D. Einstein-like approximation for phonon contribution

Let us consider a model where the electron orbital on a site fluctuates with noise characterized by a Gaussian distribution. Then the modified orbital is given as

$$\tilde{\Phi}_{\nu\mathbf{k}}(\mathbf{r}) = \int d\mathbf{x} \Phi_{\nu\mathbf{k}}(\mathbf{r} + \mathbf{x}) f(\mathbf{x}), \quad (17)$$

where $f(\mathbf{x}) = (2\pi\alpha)^{-3/2} \exp(-\frac{x^2}{2\alpha})$, ν is the band index, and $\Phi_{\nu\mathbf{k}}(\mathbf{r})$ is the original wave function. Taking the Fourier transform and making a change of variable, $\mathbf{r}' = \mathbf{r} + \mathbf{x}$, we get

$$\begin{aligned} \tilde{\Phi}_{\nu\mathbf{k}} &= \int d\mathbf{r} \tilde{\Phi}_{\nu\mathbf{k}}(\mathbf{r}) e^{-i\mathbf{k}\cdot\mathbf{r}} \\ &= \int d\mathbf{r}' \Phi_{\nu\mathbf{k}}(\mathbf{r}') e^{-i\mathbf{k}\cdot\mathbf{r}'} \int d\mathbf{x} f(\mathbf{x}) e^{i\mathbf{k}\cdot\mathbf{x}} \\ &= \Phi_{\nu\mathbf{k}} e^{-\alpha k^2/2}. \end{aligned} \quad (18)$$

Therefore, the modified momentum distribution will be $n(\mathbf{k})e^{-\alpha k^2}$, since $\sum_{\nu} |\tilde{\Phi}_{\nu\mathbf{k}}|^2 = \sum_{\nu} |\Phi_{\nu\mathbf{k}} e^{-\alpha k^2/2}|^2 = \sum_{\nu} |\Phi_{\nu\mathbf{k}}|^2 e^{-\alpha k^2} = n(\mathbf{k})e^{-\alpha k^2}$. The sum over ν only includes occupied orbitals.

III. RESULTS AND DISCUSSION

As expected due to the prior success of QMC in VO_2 , our results yield good agreement with the experimental Compton profile data [1]. For example, at $q = 0$ our values including the Hartree-Fock core contribution [85] are 10.456(4) ea_0^{-1} and 10.444(4) ea_0^{-1} for R phase and M1 phase, respectively. For the M1 phase an experimental value of 10.102(22) ea_0^{-1} and DFT-LCAO value of

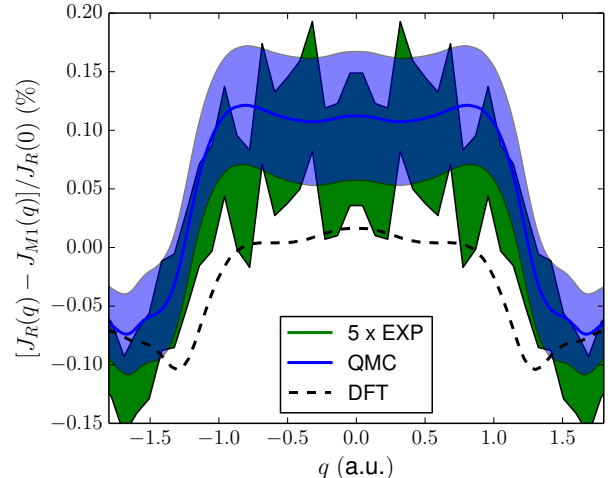


FIG. 2. Scaled Compton profile difference across the phase transition. Experimental data [26] in green have been multiplied by five in order to account for the quantitative difference in the scaled difference profile. Quantum Monte Carlo with 1σ statistical error is shown in blue (on top of the experiment), and DFT of this work (LDA+ U with DMC optimized U value, $U = 3.5$ eV) as black dashed line. In the figure we concentrate on the region in which DFT, QMC and the experiments have noticeable differences, i.e., the region of valence electron contributions.

9.761 are reported in Ref. [1], and in Ref. [26] a value of 10 ea_0^{-1} was used for $J_R(0)$. However, in general a more accurate measure both experimentally and computationally is given by considering differences between the phases since, e.g., the core contributions as well as some experimental uncertainties will cancel. Considering the subtle changes across the transition in a scaled difference profile [26], i.e., $[J_R(q) - J_{M1}(q)]/J_R(0) \times 100\%$, we find only a good qualitative correspondence. This is shown in Fig. 2. The change in the scaled difference profile is very delicate; for all q the scaled difference in $J(q)$ between the M1 and R phases remains below 0.2%. The related experimental data in Fig. 2 is multiplied by a factor of five (as in Ref. [26]) in order to obtain good quantitative correspondence in the scaled difference profile between theory and experiment. As argued by Ruotsalainen et al.[26], this effect is believed to derive from the electron-phonon coupling, which would indicate small uneven changes in the Compton profile values for the high-temperature and low-temperature phases. The change would need only to be less than 0.1% in order to account for the observed quantitative difference. Using our a simple Einstein solid-like picture we derived an on-site approximation for the electron wave function influenced by nuclear motion. Within this harmonic model the momentum distribution would include an additional phonon-related term, i.e., $n(\mathbf{k}) \rightarrow n(\mathbf{k}) \exp(-\alpha k^2)$, in which α is the variance of a Gaussian distribution in po-

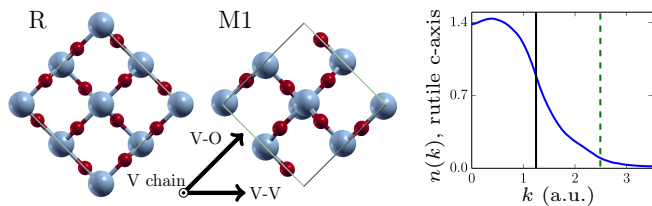


FIG. 3. Supercell crystal structures of R and M1 phases specifying directions used in the analysis. The vanadium chain direction (rutile c -axis in general) is out of plane. Subtle structural changes can be seen, e.g., the misalignment of the V atoms along the chain direction (zig-zag “chain”). On the right we show the momentum distribution in R phase along the vanadium chain direction. The statistical error bars are smaller than the line width. Vertical lines are estimates for the Fermi momentum k_F and $2k_F$ obtained from angular averaged “isotropic” momentum distribution.

sition space. Already $\alpha_R - \alpha_{M1} \approx 0.0001a_0^2$ would be enough to remove the quantitative discrepancy between theory and experiment. Therefore, a slight increase in the thermal motion and/or softening of phonon modes when going from M1 to R phase is a likely explanation for the factor of five in the difference profile. The softening of the phonon modes has been reported for example in Ref. [22]. It should be pointed out that this simple model removes the quantitative discrepancy only for a limited range, i.e., roughly $|q| < 1.0a_0^{-1}$.

In Ref. 26 it was shown that density functional theory (DFT) within LDA+U/LDA approaches results in negative scaled Compton profile differences for small momentum transfer values. In our previous study [8] we optimized the Hubbard U of LDA+U with DMC. This procedure finds the optimal U -value for trial wave function within our fixed-node DMC approach that provides a rigorous upper bound for the total energy. Interestingly, we find that this procedure also results in an improved agreement with experiments already at the DFT level, by increasing the small momentum values of $\Delta J(q)/J_R(0)$ close to zero on the positive side. The agreement is further enhanced with the more accurate correlation description provided by QMC, as shown in Fig. 2, where we show the challenging region. Outside the limits of this region all the curves are in very good agreement with each other.

In Fig. 3 we show our supercell crystal structures of the two phases and define the general directions used in the analysis of the momentum distributions. There the vanadium chain direction (or rutile c -axis) is out of plane. Subtle structural changes can be seen, e.g., the misalignment of the V atoms along the chain direction in M1 phase. There the vanadium atoms are arranged in a “zig-zag” type chain structure. Raising the temperature above the transition temperature will lead to a perfectly aligned chain along the V chain direction, and complementary changes also in the V-V and V-O directions shown in Fig. 3. In addition, in the R phase along

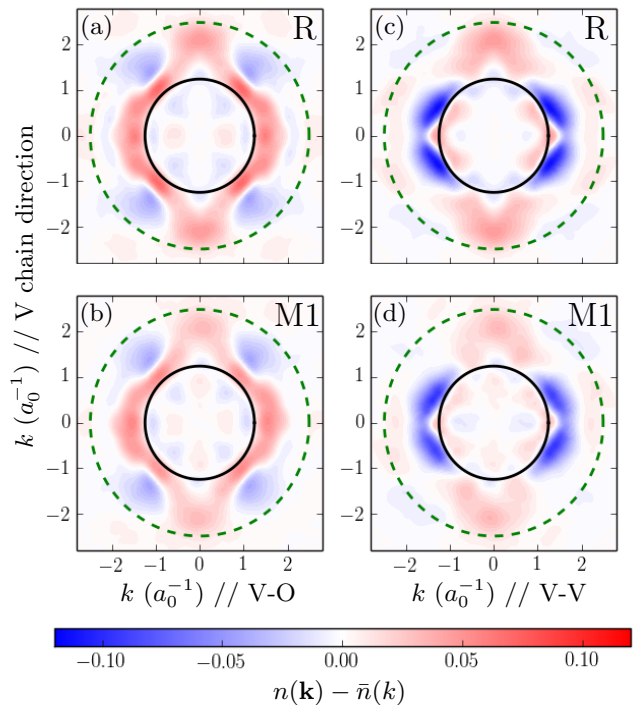


FIG. 4. Anisotropies of the momentum distribution on two different planes. Plane 1: V chain direction (y -axis) – V-O direction (x -axis) (a) R phase and (b) M1 phase. Plane 2: V chain direction (y -axis) – V-V direction (x -axis) (c) R phase and (d) M1 phase. Smaller circle is an estimate of Fermi momentum k_F from angular averaged “isotropic” momentum distribution, and larger circle is at $\sim 2k_F$.

the V chain direction the vanadium atoms are evenly spaced in contrast to the M1 phase, which increases the electron hopping amplitude along the chain [86].

On the right in Fig. 3 we show the momentum distribution in the metallic R phase along the vanadium chain direction. The statistical errorbars are smaller than the width of the line, and the vertical lines are estimates of the Fermi momentum k_F and $2k_F$. Due to the absence of a clear discontinuity the Fermi momentum is estimated by the position of the minimum value in the first derivative of the angular averaged momentum distribution. Importantly, this absence of a discontinuity indicates non-Fermi liquid behavior in the metallic rutile phase. Our result agrees with recent experimental findings [15], where the violation of the Wiedemann-Franz law was attributed to the formation of a strongly correlated, incoherent non-Fermi liquid. There the charge and heat was considered to be transported by distinct diffusive modes instead of long-lived quasiparticles. For a more detailed view on the possible source for this non-Fermi liquid behavior, we will next look into the directional characteristics of the momentum distribution in both phases and also across the transition.

In Fig. 4 we present DMC anisotropies in the momen-

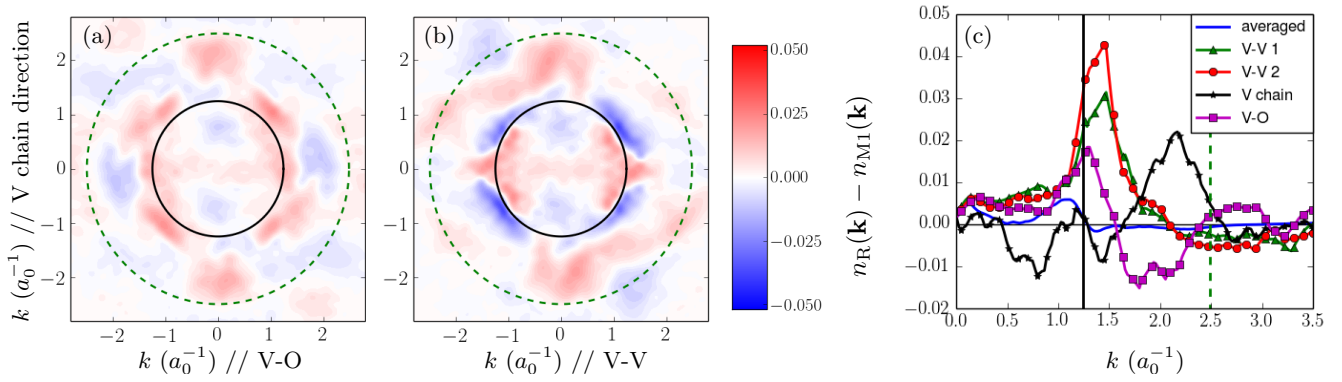


FIG. 5. Difference in the momentum distribution across the phase transition on the same two planes as in Fig. 4: (a) V chain direction (y -axis) – V-O direction (x -axis), and (b) V chain direction (y -axis) – V-V direction (x -axis). Smaller circle is an estimate of Fermi momentum k_F from angular averaged “isotropic” momentum distribution, and larger circle is at $\sim 2k_F$. In figure (c) the differences are given in four different directions and also for the angular averaged momentum distributions. In figure (c) the V-V 1 direction corresponds to the x -axis of figure (b), and V-V 2 is the direction straight up in Fig. 3, i.e., perpendicular to V-V 1.

tum distribution in two different planes for both phases: (a) R phase and (b) M1 phase are on a plane given by the rutile c -axis (V chain direction) and the V-O direction, whereas (c) R phase and (d) M1 phase are on a plane given by the rutile c -axis and the V-V direction indicated in Fig. 3. As a measure of anisotropy we use the difference $n(\mathbf{k}) - \bar{n}(k)$, where $\bar{n}(k)$ is the angular averaged momentum distribution. Comparing Figs. 4(a) and (b) we can see that the anisotropy is in general stronger in the R phase than in the M1 phase. This is rather counter-intuitive considering the differences in crystal structures of the two phases; on the other hand, it is indicative of the effects of electron-electron interactions and electron correlations. Interestingly, based on quasiparticle wave functions GW approach would indicate electronically more isotropic R phase [13]. The Seebeck coefficient measurements of Ref. [27], however, agree with our observations of noticeably larger anisotropy in the R phase. The negative Seebeck values indicate that the dominant current carriers are electrons, but according to the simple model in Ref. [27] the anisotropy can be explained if more than one type of current carrier with different and anisotropic mobilities are present. However, as we see here, the large anisotropy is present already at the electronic level. The most noticeable differences in Fig. 4 (a) and (b) are manifested along the c -axis where the R phase appears isotropic up to $\sim k_F$, with a large anisotropic contribution at $\sim 2k_F$. In the V chain – V-V plane, Figs. 4(c) and (d), the anisotropy is stronger along the “ x ”-axis than in Figs. 4(a) and (b). Moreover, apart from the chain direction the anisotropies between the planes are of different sign close to the Fermi momentum. Expressed in a similar percentage measure as the Compton profile difference in Fig. 2, i.e. $[n - \bar{n}]/n_{\max} \times 100\%$, these anisotropies would yield values up to $\sim 10\%$, which is significantly larger than the anisotropies in the Compton

profile ($< 1.2\%$ in Ref. [1]). Therefore, the anisotropies should give a clear signal in the experimental momentum distributions obtainable, e.g., through triple-differential cross section measurements [31].

In Fig. 5(a) and (b) we consider the momentum distribution across the phase transition on the same two planes as earlier in Fig. 4, whereas in Fig. 5(c) we show the difference along a few different directions as well as for the angular average. In both (a) and (b) we see that below $k < k_F$ the momentum distribution (and therefore also the average electron momentum) along the “ x ”-axis is enhanced while along the vanadium chain direction (“ y ”-axis) it is suppressed. Moreover, similar characteristics as for the anisotropies can be seen at $2k_F$ along the V-chain direction; however, in Fig. 5(b) this is more spread out than in Fig. 4. The $\sim 2k_F$ character across the phase transition can be related to an increase in Friedel oscillations as a result of back scattering, in which an electron is scattered to the opposite side of the Fermi surface; this is typical, e.g., in the context of Luttinger liquid theory, spin density waves, and electron-phonon scattering [34, 37–39]. The spatial period for Friedel oscillations would, however, be rather small to be observed, i.e., of the order of $\pi/k_F \approx 2.5a_0$, but its major contribution would be in the vanadium chain direction. In general, the $2k_F$ back scattering can lead to degradation of both the electrical and thermal currents, and is thus a likely reason for the observed anomalously low electronic thermal conductivity found fairly recently for the R phase [15]. But where does this $2k_F$ character derive from and why is it mainly observable in the V chain direction? In the Luttinger liquid model a short-range impurity will lead to Friedel oscillations that are scaled by a term including the interaction strength. Due to the absence of impurity atoms in our simulations the interactions between the rutile c -axis and directions perpendicular to it

are expected to induce “impurities” [87] resulting in the quasi-1D $\sim 2k_F$ character of these oscillations. In a rough picture this would be formed of linked one dimensional chains—essentially comprising an anisotropic component of the broader 3D electronic structure—where the links are responsible for the impurity effects. This picture is supported by the electron density considerations addressed below. The quasi-1D behavior has also been reported earlier based on GW calculations considering the role of crystal local-field and excitonic effects [14], where the quasi-1D nature was shown to influence the optical properties of VO_2 . The increased probabilities and the anisotropies observed here also support the experimental results for the Seebeck coefficients [27], which indicate a $\sim 9\%$ smaller conductivity along the rutile c -axis compared to the directions perpendicular to it. Importantly, Fig. 5 describes the electron momentum transfer in the MIT, thus providing new complementary knowledge also of phase transition.

To this end, Fig. 5 shows a considerable anisotropic shift in the momentum distribution function and change in its character: along the V-V1, V-V2, and also V-O directions there is a shift of weight towards momenta slightly larger than k_F , consistent with the formation of a more metallic-like Fermi surface in these directions. In contrast, the momentum distribution along the V-chain axis depletes weight from below the k_F and adds considerable weight out towards $2k_F$. This is indicative both of a large “smearing” of the momentum distribution function, as well as Friedel oscillations at $2k_F$, both consistent with a non-Fermi liquid like behavior along the V-chain axis. In Fig. 6 we plot electron density isoconcentration surfaces: R phase in (a) and (b), M1 phase in (c) and (d). Clear 1D chain-like isoconcentration surfaces along the V-chain directions are observed with real-space oscillations corresponding to the momentum distribution peak near $2k_F$. These plots are also consistent with 1D non-Fermi liquid-like behavior along the V-chain direction. These observations lead to the following picture: in the insulating M1 phase, dimerization along the V chains driven by correlations prevents the formation of metallicity, and the system is insulating. As the MIT is approached from the M1 phase, correlation energy diminishes (relative to other energies), allowing the formation of a Fermi surface. However, a remnant of strong correlations along the V-chain axis leads to non-Fermi-liquid like behavior along this direction. It is also insightful to consider the MIT from the metallic side. Strong correlations along the V-chain axis prevents the formation of a clear Fermi surface in those directions, leading to non-Fermi liquid-like behavior along the V-chains. As the MIT is approached from the R phase, correlation strengths increase leading to dimerization and the insulating M1 phase. In other words, the MIT is driven primarily by electronic correlations, not by structural instabilities.

In the R phase the oscillations in the electron density for the “1D chains” are identical whereas in the M1

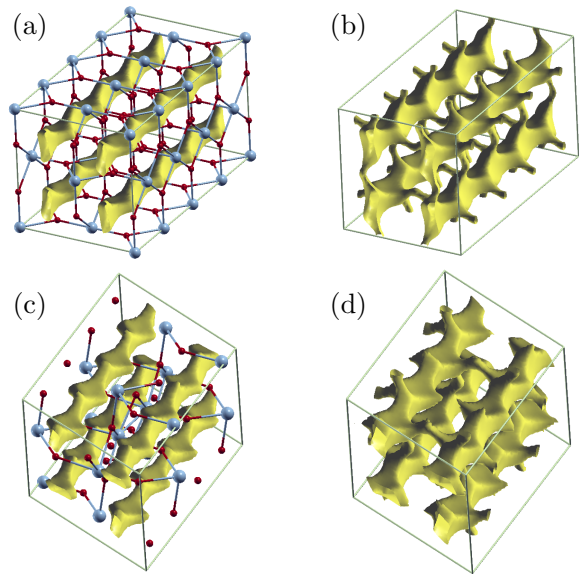


FIG. 6. Electron density isosurfaces (atomic units, e/a_0^3): (a) R phase with isovalue 0.06, (b) R phase with isovalue 0.08, (c) M1 phase with isovalue 0.06, and (d) M1 phase with isovalue 0.08. Quantum Monte Carlo electron densities are from Materials Data Facility related to Ref. 8. For clarity the atoms are not shown in (b) and (d). These figures have been made with XCrysden [88, 89].

phase they are not. Actually, in the M1 phase a nearest neighbor “1D chain” has a phase shift of half the period, which changes the positions of the maxima and minima. Slightly increasing the isovalue, i.e. going from (a) to (b), we see a formation of “links” between the chains. In the R phase the amount of these links is larger than in the M1 phase with the same isovalue. This is likely related to the enhancement of back-scattering seen in the MIT, and further supports the Luttinger picture of connected/linked “1D chains” introduced earlier.

IV. CONCLUSIONS

In this study we used first-principles quantum Monte Carlo to obtain the momentum distribution and Compton profiles for the R and M1 phases of vanadium dioxide. A good qualitative agreement with the experimental data was shown for the Compton profile differences across the metal-insulator transition. The quantitative differences are considered to arise from electron-phonon coupling based on a simple theoretical model and experimental observations [26]. Analysis of the momentum distribution reveals the signature of the non-Fermi liquid character of the metallic R phase proposed by recent experiments [15]. Moreover, we observe that Friedel oscillations in the R phase are mainly confined in one-dimension, which together with the observed $\sim 2k_F$ characteristics are reminiscent of a Luttinger liquid type metal with impurities. These impurities could emerge as a consequence of

the transverse dimensions. In addition, we believe that our findings provide an explanation for the experimentally observed anomalously low electronic thermal conductivity [15], as we observe back scattering characteristics within the momentum distribution.

V. ACKNOWLEDGMENTS

We thank K. Ruotsalainen et al. [26] for providing the experimental data, and David Ceperley, Yubo Yang, and Anshul Kogar for useful comments. This work was supported by the U.S. Department of Energy, Office of Science, Basic Energy Sciences, Materials Sciences and En-

gineering Division, as part of the Computational Materials Sciences Program and Center for Predictive Simulation of Functional Materials. An award of computer time was provided by the Innovative and Novel Computational Impact on Theory and Experiment (INCITE) Program. This research used resources of the Argonne Leadership Computing Facility, which is a U.S. Department of Energy Office of Science User Facility operated under contract DE-AC02-06CH11357, and the resources of the Oak Ridge Leadership Computing Facility at the Oak Ridge National Laboratory, which is supported by the Office of Science of the U.S. Department of Energy under Contract No. DE-AC05-00OR22725.

-
- [1] M. Vashistha, D. R. Phalaswal, K. Kabra, R. Kumar, B. K. Sharma, and G. Sharma, *Materials Focus* **5**, 517 (2016).
 - [2] M. Imada, A. Fujimori, and Y. Tokura, *Rev. Mod. Phys.* **70**, 1039 (1998).
 - [3] Z. Zhang, F. Zuo, C. Wan, A. Dutta, J. Kim, J. Rensberg, R. Nawrodt, H. H. Park, T. J. Larrabee, X. Guan, Y. Zhou, S. M. Prokes, C. Ronning, V. M. Shalaev, A. Boltasseva, M. A. Kats, and S. Ramanathan, *Phys. Rev. Applied* **7**, 034008 (2017).
 - [4] A. Zylbersztein and N. F. Mott, *Phys. Rev. B* **11**, 4383 (1975).
 - [5] V. Eyert, *Annalen der Physik* **11**, 650 (2002).
 - [6] Z. Zhu and U. Schwingenschlöggl, *Phys. Rev. B* **86**, 075149 (2012).
 - [7] R. Grau-Crespo, H. Wang, and U. Schwingenschlöggl, *Phys. Rev. B* **86**, 081101 (2012).
 - [8] I. Kylänpää, J. Balachandran, P. Ganesh, O. Heinonen, P. R. C. Kent, and J. T. Krogel, *Phys. Rev. Materials* **1**, 065408 (2017).
 - [9] H. Zheng and L. K. Wagner, *Phys. Rev. Lett.* **114**, 176401 (2015).
 - [10] S. Biermann, A. Poteryaev, A. I. Lichtenstein, and A. Georges, *Phys. Rev. Lett.* **94**, 026404 (2005).
 - [11] J. M. Tomczak, F. Aryasetiawan, and S. Biermann, *Phys. Rev. B* **78**, 115103 (2008).
 - [12] W. H. Brito, M. C. O. Aguiar, K. Haule, and G. Kotliar, *Phys. Rev. Lett.* **117**, 056402 (2016).
 - [13] M. Gatti, F. Bruneval, V. Olevano, and L. Reining, *Phys. Rev. Lett.* **99**, 266402 (2007).
 - [14] M. Gatti, F. Sottile, and L. Reining, *Phys. Rev. B* **91**, 195137 (2015).
 - [15] S. Lee, K. Hippalgaonkar, F. Yang, J. Hong, C. Ko, J. Suh, K. Liu, K. Wang, J. J. Urban, X. Zhang, C. Dames, S. A. Hartnoll, O. Delaire, and J. Wu, *Science* **355**, 371 (2017).
 - [16] Y. Chen, S. Zhang, F. Ke, C. Ko, S. Lee, K. Liu, B. Chen, J. W. Ager, R. Jeanloz, V. Eyert, and J. Wu, *Nano Letters* **17**, 2512 (2017).
 - [17] D. Y. Lei, K. Appavoo, F. Ligmajer, Y. Sonnefraud, R. F. Haglund, and S. A. Maier, *ACS Photonics* **2**, 1306 (2015).
 - [18] W. A. Vitale, M. Tamagnone, N. Émond, B. L. Drogoff, S. Capdevila, A. Skrivervik, M. Chaker, J. R. Mosig, and A. M. Ionescu, *Scientific Reports* **7**, 41546 (2017).
 - [19] W. A. Vitale, E. A. Casu, A. Biswas, T. Rosca, C. Alper, A. Krammer, G. V. Luong, Q.-T. Zhao, S. Mantl, A. Schüler, and A. M. Ionescu, *Scientific Reports* **7**, 355 (2017).
 - [20] D. W. Ferrara, J. Nag, E. R. MacQuarrie, A. B. Kaye, and R. F. Haglund, *Nano Letters* **13**, 4169 (2013).
 - [21] J. Holleman, M. M. Bishop, C. Garcia, J. S. R. Vellore Winfred, S. Lee, H. N. Lee, C. Beekman, E. Manousakis, and S. A. McGill, *Phys. Rev. B* **94**, 155129 (2016).
 - [22] J. D. Budai, J. Hong, M. E. Manley, E. D. Specht, C. W. Li, J. Z. Tischler, D. L. Abernathy, A. H. Said, B. M. Leu, L. A. Boatner, R. J. McQueeney, and O. Delaire, *Nature* **515**, 535 (2014).
 - [23] F. J. Morin, *Phys. Rev. Lett.* **3**, 34 (1959).
 - [24] A. Tselev, I. A. Lukyanchuk, I. N. Ivanov, J. D. Budai, J. Z. Tischler, E. Strelcov, A. Kolmakov, and S. V. Kalinin, *Nano Letters* **10**, 4409 (2010).
 - [25] M. A. Huber, M. Plankl, M. Eisele, R. E. Marvel, F. Sandner, T. Korn, C. Schiller, R. F. Haglund, R. Huber, and T. L. Cocker, *Nano Letters* **16**, 1421 (2016).
 - [26] K. O. Ruotsalainen, J. Inkinen, T. Pylkkänen, T. Buslaps, M. Hakala, K. Hämäläinen, and S. Huotari, *The European Physical Journal B* **91**, 225 (2018).
 - [27] C. N. Berglund and H. J. Guggenheim, *Phys. Rev.* **185**, 1022 (1969).
 - [28] P. Lindner, *Physica Scripta* **15**, 112 (1977).
 - [29] B. G. Williams, *Physica Scripta* **15**, 92 (1977).
 - [30] M. J. Cooper, *Reports on Progress in Physics* **48**, 415 (1985).
 - [31] F. Bell and J. R. Schneider, *Journal of Physics: Condensed Matter* **13**, 7905 (2001).
 - [32] R. N. Silver and P. E. Sokol, eds., *Momentum Distributions* (Plenum Press, New York, 1989).
 - [33] F. Zambelli, L. Pitaevskii, D. M. Stamper-Kurn, and S. Stringari, *Phys. Rev. A* **61**, 063608 (2000).
 - [34] S. B. Dugdale, *Physica Scripta* **91**, 053009 (2016).
 - [35] S. Huotari, J. A. Soimin, T. Pylkkänen, K. Hämäläinen, A. Issolah, A. Titov, J. McMinis, J. Kim, K. Esler, D. M. Ceperley, M. Holzmann, and V. Olevano, *Phys. Rev. Lett.* **105**, 086403 (2010).
 - [36] M. Holzmann, B. Bernu, C. Pierleoni, J. McMinis, D. M. Ceperley, V. Olevano, and L. Delle Site, *Phys. Rev. Lett.*

- 107**, 110402 (2011).
- [37] K. Schönhammer, *Strong interactions in low dimensions*, edited by D. Baeriswyl and L. Degiorgi, Vol. 25 (Springer, 2004) Luttinger liquids: the basic concepts.
 - [38] S.-i. Tomonaga, *Progress of Theoretical Physics* **5**, 544 (1950).
 - [39] J. M. Luttinger, *Journal of Mathematical Physics* **4**, 11541162 (1963).
 - [40] Hiraoka N. and Nomura T., *Scientific Reports* **7**, 565 (2017).
 - [41] C. Filippi and D. M. Ceperley, *Phys. Rev. B* **59**, 7907 (1999).
 - [42] W. M. C. Foulkes, L. Mitas, R. J. Needs, and G. Rajagopal, *Rev. Mod. Phys.* **73**, 33 (2001).
 - [43] J. Kim, A. T. Baczewski, T. D. Beaudet, A. Benali, M. C. Bennett, M. A. Berrill, N. S. Blunt, E. J. L. Borda, M. Casula, D. M. Ceperley, S. Chiesa, B. K. Clark, R. C. C. III, K. T. Delaney, M. Dewing, K. P. Esler, H. Hao, O. Heinonen, P. R. C. Kent, J. T. Krogel, I. Kylänpää, Y. W. Li, M. G. Lopez, Y. Luo, F. D. Malone, R. M. Martin, A. Mathuriya, J. McMinis, C. A. Melton, L. Mitas, M. A. Morales, E. Neuscamman, W. D. Parker, S. D. P. Flores, N. A. Romero, B. M. Rubenstein, J. A. R. Shea, H. Shin, L. Shulenburger, A. F. Tillack, J. P. Townsend, N. M. Tubman, B. V. D. Goetz, J. E. Vincent, D. C. Yang, Y. Yang, S. Zhang, and L. Zhao, *Journal of Physics: Condensed Matter* **30**, 195901 (2018).
 - [44] N. M. Tubman, I. Kylänpää, S. Hammes-Schiffer, and D. M. Ceperley, *Phys. Rev. A* **90**, 042507 (2014).
 - [45] Y. Yang, I. Kylänpää, N. M. Tubman, J. T. Krogel, S. Hammes-Schiffer, and D. M. Ceperley, *J. Chem. Phys.* **143**, 124308 (2015).
 - [46] C. J. Umrigar, M. P. Nightingale, and K. J. Runge, *J. Chem. Phys.* **99**, 2865 (1993).
 - [47] J. B. Anderson, *J. Chem. Phys.* **63**, 1499 (1975).
 - [48] D. M. Ceperley and B. J. Alder, *Phys. Rev. Lett.* **45**, 566 (1980).
 - [49] L. K. Wagner and D. M. Ceperley, *Rep. Prog. Phys.* **79**, 094501 (2016).
 - [50] L. K. Wagner, *J. Phys.: Condens. Matter* **19**, 343201 (2007).
 - [51] J. Kolorenč and L. Mitas, *Phys. Rev. Lett.* **101**, 185502 (2008).
 - [52] L. Mitas and J. Kolorenč, *Reviews in Mineralogy and Geochemistry* **71**, 137 (2010).
 - [53] J. Kolorenč, S. Hu, and L. Mitas, *Phys. Rev. B* **82**, 115108 (2010).
 - [54] K. Foyevtsova, J. T. Krogel, J. Kim, P. R. C. Kent, E. Dagotto, and F. A. Reboredo, *Phys. Rev. X* **4**, 031003 (2014).
 - [55] L. K. Wagner and P. Abbamonte, *Phys. Rev. B* **90**, 125129 (2014).
 - [56] J. Yu, L. K. Wagner, and E. Ertekin, *J. Chem. Phys.* **143**, 224707 (2015).
 - [57] J. A. Schiller, L. K. Wagner, and E. Ertekin, *Phys. Rev. B* **92**, 235209 (2015).
 - [58] L. K. Wagner, *Phys. Rev. B* **92**, 161116 (2015).
 - [59] Y. Luo, A. Benali, L. Shulenburger, J. T. Krogel, O. Heinonen, and P. R. C. Kent, *New Journal of Physics* **18**, 113049 (2016).
 - [60] J. A. Santana, J. T. Krogel, P. R. C. Kent, and F. A. Reboredo, *J. Chem. Phys.* **144**, 174707 (2016).
 - [61] A. Benali, L. Shulenburger, J. T. Krogel, X. Zhong, P. R. C. Kent, and O. Heinonen, *Phys. Chem. Chem. Phys.* **18**, 18323 (2016).
 - [62] K. Doblhoff-Dier, J. Meyer, P. E. Hoggan, G.-J. Kroes, and L. K. Wagner, *J. Chem. Theory Comput.* **12**, 2583 (2016).
 - [63] J. Trail, B. Monserrat, P. López Ríos, R. Maezono, and R. J. Needs, *Phys. Rev. B* **95**, 121108 (2017).
 - [64] J. Yu, L. K. Wagner, and E. Ertekin, *Phys. Rev. B* **95**, 075209 (2017).
 - [65] M. Holzmann, B. Bernu, and D. M. Ceperley, *Journal of Physics: Conference Series* **321**, 012020 (2011).
 - [66] J. Longo and P. Kierkegaard, *Acta Chemica Scandinavica* **24**, 420 (1970).
 - [67] M. Ghedira, H. Vincent, M. Marezio, and J. Launay, *J. Solid State Chem.* **22**, 423 (1977).
 - [68] M. Hellenbrandt, *Crystallography Reviews* **10**, 17 (2004).
 - [69] B. Blaiszik, K. Chard, J. Pruyne, R. Ananthakrishnan, S. Tuecke, and I. Foster, *JOM* **68**, 2045 (2016).
 - [70] P. Giannozzi, S. Baroni, N. Bonini, M. Calandra, R. Car, C. Cavazzoni, D. Ceresoli, G. L. Chiarotti, M. Cococcioni, I. Dabo, A. Dal Corso, S. de Gironcoli, S. Fabris, G. Fratesi, R. Gebauer, U. Gerstmann, C. Gougoussis, A. Kokalj, M. Lazzeri, L. Martin-Samos, N. Marzari, F. Mauri, R. Mazzarello, S. Paolini, A. Pasquarello, L. Paulatto, C. Sbraccia, S. Scandolo, G. Sclauzero, A. P. Seitsonen, A. Smogunov, P. Umari, and R. M. Wentzcovitch, *J. Phys.: Condensed Matter* **21**, 395502 (2009).
 - [71] J. Kim, K. P. Esler, J. McMinis, M. A. Morales, B. K. Clark, L. Shulenburger, and D. M. Ceperley, *J. Phys. Conf. Ser.* **402**, 012008 (2012).
 - [72] C. Lin, F. H. Zong, and D. M. Ceperley, *Phys. Rev. E* **64**, 016702 (2001).
 - [73] J. C. Slater, *Phys. Rev.* **34**, 1293 (1929).
 - [74] R. Jastrow, *Phys. Rev.* **98**, 1479 (1955).
 - [75] N. D. Drummond, M. D. Towler, and R. J. Needs, *Phys. Rev. B* **70**, 235119 (2004).
 - [76] C. J. Umrigar, J. Toulouse, C. Filippi, S. Sorella, and R. G. Hennig, *Phys. Rev. Lett.* **98**, 110201 (2007).
 - [77] M. M. Hurley and P. A. Christiansen, *J. Chem. Phys.* **86**, 10691070 (1987).
 - [78] L. Mitas, E. L. Shirley, and D. M. Ceperley, *J. Chem. Phys.* **95**, 34673475 (1991).
 - [79] M. Casula, *Phys. Rev. B* **74**, 161102 (2006).
 - [80] C. J. Umrigar and C. Filippi, *Phys. Rev. Lett.* **94**, 150201 (2005).
 - [81] J. B. Anderson, *J. Chem. Phys.* **63**, 1499 (1975).
 - [82] J. B. Anderson, *J. Chem. Phys.* **65**, 4121 (1976).
 - [83] G. Ortiz, D. M. Ceperley, and R. M. Martin, *Phys. Rev. Lett.* **71**, 2777 (1993).
 - [84] M. Casula, C. Filippi, and S. Sorella, *Phys. Rev. Lett.* **95**, 100201 (2005).
 - [85] F. Biggs, L. Mendelsohn, and J. Mann, *Atomic Data and Nuclear Data Tables* **16**, 201309 (1975).
 - [86] E. Caruthers and L. Kleinman, *Phys. Rev. B* **7**, 3760 (1973).
 - [87] C. L. Kane and M. P. A. Fisher, *Phys. Rev. Lett.* **76**, 3192 (1996).
 - [88] A. Kokalj, *Comp. Mater. Sci.* **28**, 155 (2003).
 - [89] A. Kokalj, *J. Mol. Graphics Modelling* **17**, 176 (1999).

TABLE I. Primitive cell axes and atomic positions in Å used in density functional theory calculations. These are experimental structures: for M1 phase we use the ICSD collection code entry 34033, and for R phase the ICSD entry 1504. Vanadium sites with up/down magnetic moment are labeled V1/V2.

	M1 phase (P2 ₁ /c)			R phase (P4 ₂ /mm)		
	<i>x</i>	<i>y</i>	<i>z</i>	<i>x</i>	<i>y</i>	<i>z</i>
<i>a</i>	5.752000000	0.000000000	0.000000000	4.554600000	0.000000000	0.000000000
<i>b</i>	0.000000000	4.537800000	0.000000000	0.000000000	4.554600000	0.000000000
<i>c</i>	-2.903573350	0.000000000	4.532170350	0.000000000	0.000000000	5.705600000
V1	1.300602890	4.442233932	0.119921229	0.000000000	0.000000000	0.000000000
V2	1.547823771	0.095566070	4.412249122	0.000000000	0.000000000	2.852799999
V1	-0.151183780	2.364466069	2.386006401	2.277299999	2.277299999	1.426399997
V2	2.999610442	2.173333934	2.146163949	2.277299999	2.277299999	4.279200001
O	0.005176999	0.961559820	0.945410729	1.366835461	1.366835461	0.000000000
O	2.843249652	3.576240182	3.586759611	3.187764536	3.187764536	0.000000000
O	-1.446609671	1.307340179	3.211495912	3.644135460	0.910464538	1.426399997
O	4.295036333	3.230459824	1.320674439	0.910464538	3.644135460	1.426399997
O	1.436088279	3.188258280	1.354212500	1.366835461	1.366835461	2.852799999
O	1.412338372	1.349541722	3.177957851	3.187764536	3.187764536	2.852799999
O	-0.015698391	3.618441721	3.620297683	3.644135460	0.910464538	4.279200001
O	2.864125042	0.919358281	0.911872668	0.910464538	3.644135460	4.279200001

TABLE II. Supercell axes and atomic positions in Å used in quantum Monte Carlo simulations.

	M1 phase			R phase		
	x	y	z	x	y	z
a	11.50400000	0.00000000	0.00000000	4.55460000	-4.55460000	0.00000000
b	2.90357335	4.53780000	-4.53217035	4.55460000	4.55460000	0.00000000
c	-2.90357335	4.53780000	4.53217035	0.00000000	0.00000000	11.41120000
V1	1.30060289	4.44223393	0.11992123	0.00000000	0.00000000	0.00000000
V2	4.45139712	4.63336607	-0.11992123	0.00000000	0.00000000	2.85280000
V1	2.75238957	6.90226607	-2.14616395	4.55460000	0.00000000	0.00000000
V2	2.99961044	2.17333393	2.14616395	4.55460000	0.00000000	2.85280000
V1	7.05260289	4.44223393	0.11992123	0.00000000	0.00000000	5.70560000
V2	10.20339712	4.63336607	-0.11992123	0.00000000	0.00000000	8.55840000
V1	8.50438957	6.90226607	-2.14616395	4.55460000	0.00000000	5.70560000
V2	8.75161044	2.17333393	2.14616395	4.55460000	0.00000000	8.55840000
V1	4.20417624	4.44223393	-4.41224912	2.27730000	2.27730000	1.42640000
V2	1.54782377	4.63336607	4.41224912	2.27730000	2.27730000	4.27920000
V1	2.75238957	2.36446607	-2.14616395	2.27730000	-2.27730000	1.42640000
V2	2.99961044	6.71113393	2.14616395	2.27730000	-2.27730000	4.27920000
V1	9.95617624	4.44223393	-4.41224912	2.27730000	2.27730000	7.13200000
V2	7.29982377	4.63336607	4.41224912	2.27730000	2.27730000	9.98480000
V1	8.50438957	2.36446607	-2.14616395	2.27730000	-2.27730000	7.13200000
V2	8.75161044	6.71113393	2.14616395	2.27730000	-2.27730000	9.98480000
O	0.00517700	0.96155982	0.94541073	1.36683546	1.36683546	0.00000000
O	5.74682300	8.11404018	-0.94541074	3.18776454	3.18776454	0.00000000
O	1.45696368	5.84514018	-1.32067444	3.64413546	0.91046454	1.42640000
O	4.29503633	3.23045982	1.32067444	5.46506454	-0.91046454	1.42640000
O	1.43608828	3.18825828	1.35421250	1.36683546	1.36683546	2.85280000
O	4.31591172	5.88734172	-1.35421250	3.18776454	3.18776454	2.85280000
O	2.88787496	8.15624172	-0.91187267	3.64413546	0.91046454	4.27920000
O	2.86412504	0.91935828	0.91187267	5.46506454	-0.91046454	4.27920000
O	5.75717700	0.96155982	0.94541073	5.92143546	1.36683546	0.00000000
O	11.49882300	8.11404018	-0.94541074	3.18776454	-1.36683546	0.00000000
O	7.20896368	5.84514018	-1.32067444	3.64413546	-3.64413546	1.42640000
O	10.04703633	3.23045982	1.32067444	0.91046454	-0.91046454	1.42640000
O	7.18808828	3.18825828	1.35421250	5.92143546	1.36683546	2.85280000
O	10.06791172	5.88734172	-1.35421250	3.18776454	-1.36683546	2.85280000
O	8.63987496	8.15624172	-0.91187267	3.64413546	-3.64413546	4.27920000
O	8.61612504	0.91935828	0.91187267	0.91046454	-0.91046454	4.27920000
O	0.00517700	5.49935982	0.94541073	1.36683546	1.36683546	5.70560000
O	5.74682300	3.57624018	-0.94541074	3.18776454	3.18776454	5.70560000
O	-1.44660967	5.84514018	3.21149591	3.64413546	0.91046454	7.13200000
O	7.19860968	3.23045982	-3.21149591	5.46506454	-0.91046454	7.13200000
O	4.33966163	3.18825828	-3.17795785	1.36683546	1.36683546	8.55840000
O	1.41233837	5.88734172	3.17795785	3.18776454	3.18776454	8.55840000
O	2.88787496	3.61844172	-0.91187267	3.64413546	0.91046454	9.98480000
O	2.86412504	5.45715828	0.91187267	5.46506454	-0.91046454	9.98480000
O	5.75717700	5.49935982	0.94541073	5.92143546	1.36683546	5.70560000
O	11.49882300	3.57624018	-0.94541074	3.18776454	-1.36683546	5.70560000
O	4.30539033	5.84514018	3.21149591	3.64413546	-3.64413546	7.13200000
O	12.95060968	3.23045982	-3.21149591	0.91046454	-0.91046454	7.13200000
O	10.09166163	3.18825828	-3.17795785	5.92143546	1.36683546	8.55840000
O	7.16433837	5.88734172	3.17795785	3.18776454	-1.36683546	8.55840000
O	8.63987496	3.61844172	-0.91187267	3.64413546	-3.64413546	9.98480000
O	8.61612504	5.45715828	0.91187267	0.91046454	-0.91046454	9.98480000